# Assessing Impacts on Pressure Stabilization and Leasing Acreage for $CO_2$ Storage Using Utilizing Oil Migration Concepts

Melianna Ulfah[a], Seyyed Hosseini[b], Susan Hovorka[b], Alex Bump[b], Sahar Bakhshian[b], Dallas Dunlap[b]

[a]*Jackson School of Geosciences, The University of Texas Austin, Austin, TX 78712*
[b]*Gulf Coast Carbon Center, Bureau of Economic Geology, 10611 Exploration Way, Austin, TX 78758*

**Abstract**

Favorable geological storage for $CO_2$ has long been pictured as large anticlines with thick sandstones, similar to oil reservoirs in the petroleum system. Unlike oil, however, stored $CO_2$ does not need to be recoverable, which raises the possibility of using dissolution and residual trapping to augment the capacity of buoyant traps and tap more of the bulk rock volume. The work presented builds on that idea, asking the following question: If we inject $CO_2$ down to a syncline – analogous to the carrier bed in the petroleum system – how would this injection mechanism impact storage capacity and plume shape, migration, and stabilization? To address this question, we built a reservoir model, based on seismic interpretation of Middle Miocene strata, offshore Galveston, Texas. 3-D seismic and well logs were used to characterize key intervals. Reservoirs chosen for modeling are progradational-aggradational sands with mud intercalation. They have a higher degree of heterogeneity than the more conventional reservoirs commonly targeted for $CO_2$ storage. Modeling investigated how far the $CO_2$ plume would migrate under two scenarios: (1) injecting $CO_2$ at the base of the salt withdrawal basin (syncline scenario) and (2) injecting $CO_2$ at the base of the structural closure, similar to a common injection well location for EOR purposes (base scenario). For each scenario, we separately simulated injection of 30 MT of $CO_2$ and 60 MT of $CO_2$ continuously for 30 years and observe the plume and pressure evolution for 100 years after the injection stops. The simulation shows that injecting the $CO_2$ into a syncline limits the vertical migration of $CO_2$, thus making synclinal injection more secure. In the syncline scenario, the geological layer around the injection point is more heterogeneous than the layer in the base scenario; thus, the $CO_2$ tends to migrate laterally. Additionally, in the syncline scenario, the plume does not even reach the upper part of the anticline, allowing us to safely store an additional amount of $CO_2$ into the reservoir. Moreover, the simulation also shows that in the syncline scenario, the times needed for the reservoir to reach its stabilized pressure after the end of injections are faster. To summarize, $CO_2$ injection at the base of a syncline could provide additional storage, increase the safety of the project from the limited vertical plume migration, and expedite plume stabilization, which could result in the decrease of monitoring frequency as the project runs, thus lowering the operating cost of the project in the long run.

*Keywords: $CO_2$ storage; migration; plume stabilization; plume shape; pressure decay; heterogeneity; leasing acreage*

## 1. Introduction and Previous Work

Favorable geological storage to trap and retain $CO_2$ in the subsurface can play a significant role in mitigating carbon emissions. The migration pathway is important in subsurface $CO_2$ storage in that it impacts the fraction of $CO_2$ being retained within the pore space and thus being permanently trapped. Several studies have been attempted to demonstrate how the stratigraphic or structural traps and petrophysical properties impact the $CO_2$ migration during and after the injection process. A previous study simulated $CO_2$ injections into an open-boundary and sand-rich deltaic system, showing that only 0.03-21% of 1 MT of $CO_2$ is being retained and the retained volume increases as the migration pathway lengthens (Beckham, 2018). Another study shows that incorporating heterogeneity into a numerical simulation model adds local capillary trapping to the simulation model, and the result shows how a trapping mechanism could eventually stop the migration of the $CO_2$ plume up-dip (Hosseininoosheri, 2019).

Another numerical modeling case was presented by Cavanagh and Haszeldine (2014) who investigated the nature of $CO_2$ trapping and dispersal beneath the caprock using the Sleipner benchmark model to challenge and improve numerical and analytical flow modeling. Using pressure-compensated Darcy flow and capillary flow, Cavanagh and Haszeldine's study shows that a black oil reservoir model derives the best match to the plume shape acquired from seismic data obtained in 2006 and 2008, although the model only applies when adapted to approximate the near-equilibrium pressure conditions of a migration simulator for flow beneath the caprock. The study also shows dissolution over decades, resulting in substantial plume mass reduction, thus significantly decreasing the risk of post-injection lateral migration.

Another simulation work with real-world data was undertaken by CO2CRC by integrating monitoring data to refine the static and dynamic models for future field development and to offer added assurance about the long-term stabilization of the $CO_2$ plume (Dance et al, 2019). The geologic formation of interest was regarded as extremely heterogeneous, and prior to this study, probabilities varied widely about the interconnectivity of sand facies between wells. The study used time-lapse seismic data and updated permeability distribution with history matching of pressure data to provide further evidence to support the interpretation of the parasequences as being continuous across the site. This continuity added confidence that the associated flooding surfaces provide a sufficient barrier to prevent vertical flow, thus reducing prior uncertainties about the geological structure and the distribution of permeability. The improved static and dynamics model was shown to add assurance about the long-term stabilization of a $CO_2$ plume and to influence long-term monitoring strategies.

Additionally, important conclusions have emerged from other previous works that demonstrate the impact of geological heterogeneity on $CO_2$ plume distribution and migration. A previous study concluded that flow through a heterogeneous layer disperses the flow paths, contacting a larger percentage of the rock volume, and therefore increasing storage capacity (Hovorka et al., 2004). Furthermore, Ni et al. (2019) demonstrated that CO2 residual trapping ability increases with the degree of heterogeneity. Trevisan et al. (2016) also tested the idea that geological heterogeneity could moderate the plume vertical movement as it applies a major control on the plume migration and trapping mechanism, leading to delayed vertical migration and immobilization of a larger portion of $CO_2$ within coarser sediment.

In this study, we experimented with the storage lithology selection and injection scenario to better understand how the migration pathway could increase the retention of $CO_2$ in the subsurface. In the petroleum system, hydrocarbon generally moves along well-defined pathways from source rock to reservoirs and volumetric changes occur during the migration (**Fig. 1**) (Zhang et al., 2006). We tested that idea by injecting $CO_2$ down into the synclinal structure and observed how the migration loss of $CO_2$ during flow to the anticlinal structure occurs.

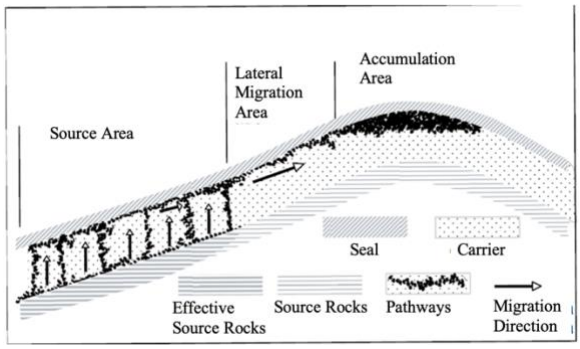


**Fig. 1.** Diagrammatic representation of migration pathways (modified from Zhang et al, 2006)

## 2. Study Area and Approach

### *2.1. Geological Setting and Limitations*

Using the complex geologic environments of the Gulf of Mexico, we performed seismic and well-log interpretation to build a porosity and permeability model. The site selected for this study comprises Middle Miocene strata, particularly an interval between the Maximum Flooding Surface (MFS) 6 to MFS 7 offshore of Galveston, Texas.

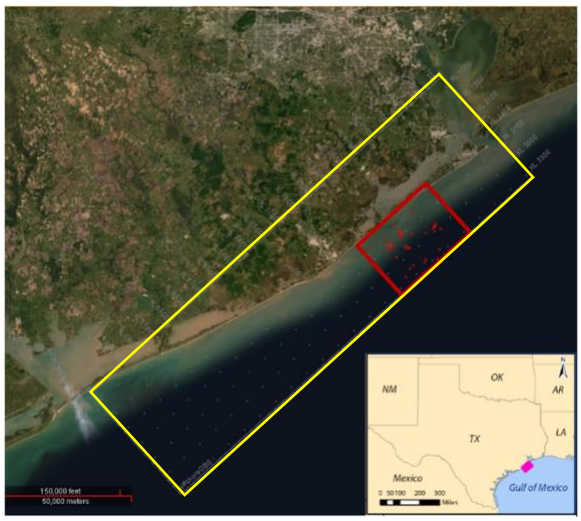


**Fig. 2.** Satellite imagery showing the area of interest indicated by the red box. Red + symbols represent the locations of well logs used in this study and the yellow box represents the regional extent of the seismic survey of the data.

The two main geological features in this study area are the salt withdrawal minibasin and turtle anticline. Salt withdrawal minibasins are relatively small (1 to 10 km across) regions filled with sediments that subside into a larger salt body (Hudec et al., 2009). As the subsidence that contains denser sediments move downwards, the less dense salt moves upward

causing the net lowering of the center of mass and causing energy to drive the subsidence and the movement of salt (Ramberg, 1981). Salt withdrawal basins are common in many salt provinces around the world including passive margins such as the Gulf of Mexico.

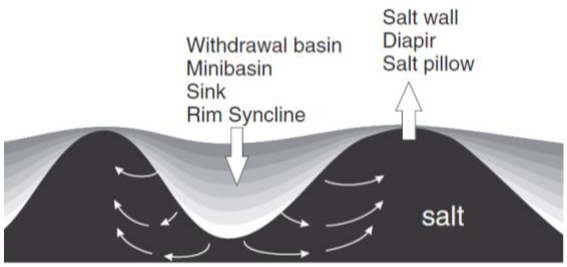


**Fig. 3.** Basic elements of a salt-withdrawal basin, showing alternative names for the region of salt depletion (minibasin) and the region of salt accumulation (Peel, 2014).

The formation of salt withdrawal basin and turtle anticline in the study area started from the early deposition of Jurassic evaporites produced a thick layer of Louann Salt found allochthonously and autochthonously throughout the northwestern Gulf of Mexico (Diegel et al, 1995). Beneath the present inner-shelf surface, the lower Miocene Clemente-Tomas and middle Miocene Corsair fault systems lie basinward. The Lower Miocene regressive episode of shelf growth then further caused the growth faulting, allowing progradation of the shelf margin farther to the southeast and into the Corsair growth fault trend (Bradshaw and Watkins, 1994). The progradation further lowered the center of mass and caused energy to drive the subsidence and with large extension, causing the diapir to part into two halves. As the extension intensified, the two halves of a diapir moved completely apart, allowing a minibasin to subside onto the base of salt, forming a bucket caused by the movement of Louann salt (Jackson and Hudec, 2017). As sea level continued to fall and the shallow marine minibasins subsided, the sediment supplied from the Corsair delta prograded across the shelf introducing a large influx of sediments into the relatively starved minibasins that pinched the less dense salt from under the subsiding region (Peel, 2014). A turtle anticline started to form as a result of continuing extension that allows the flanks of the minibasin to subside. The base of the minibasin was further bounded by a bowl-shaped weld as the salt expulsion continued, greatly thinning the original salt under the minibasin and turtle anticline and eventually moved upward forming the San Luis salt dome.

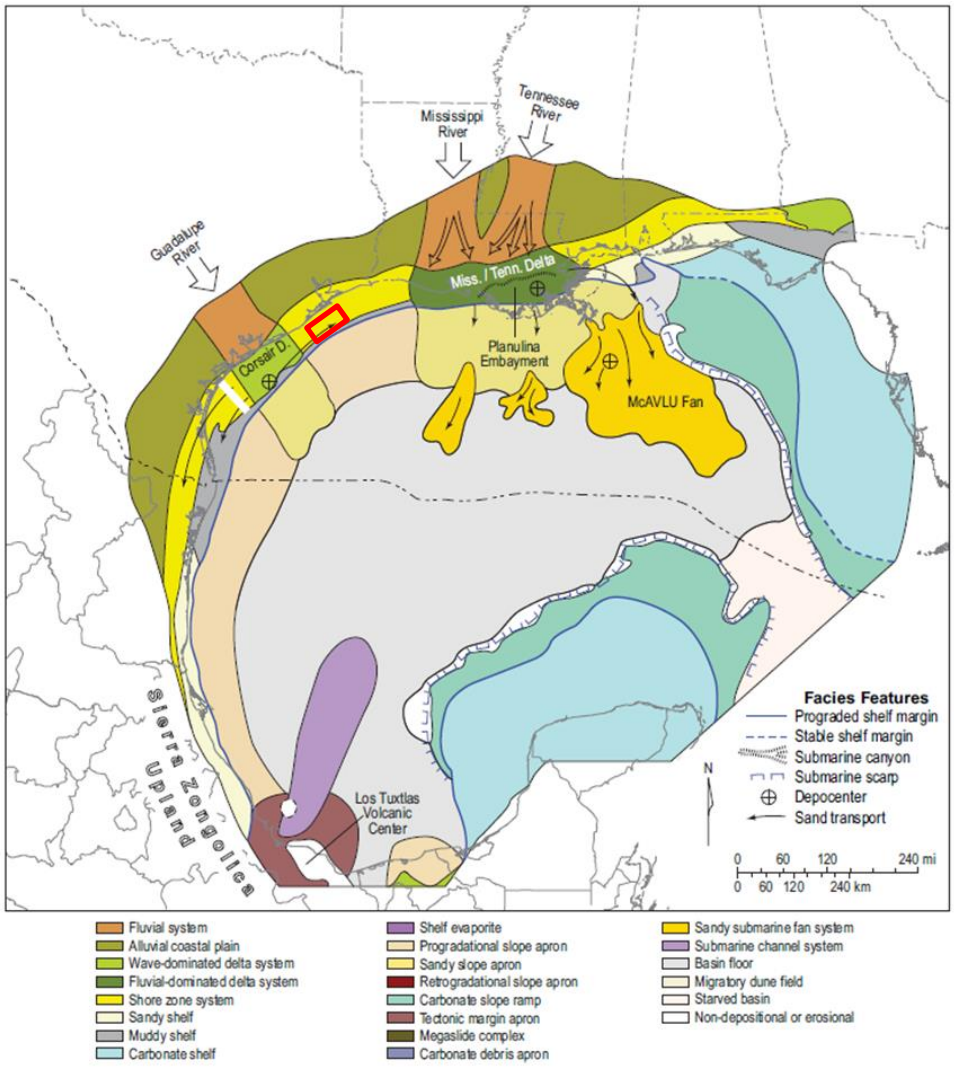


**Fig. 4.** Paleogeographic map of the middle Miocene deposode. Red box shows the study area of this project (modified from Snedden and Galloway 2019).

The synclinal structure that became the injection target in this study is a salt-withdrawal minibasin located south to southwest of the San Luis salt dome. East to southeast of the minibasin is a turtleback structure connected to the minibasins that act as the structural trap (**Fig. 10** and **Fig. 11**). Fault seal analysis is not within the scope of this study and therefore we will not evaluate whether the faults in the anticline will seal or leak the $CO_2$. Fluid flow in the salt area is also beyond the scope of this study and to incorporate a no-flow boundary, the salt dome was excluded from the model.

### *2.2. Lithotype Classification and Porosity and Permeability Calculation from Well Log*

The stratigraphy of the interval of interest was determined from 41 well logs. Our goal was to analyze the distribution of sand and shale throughout the study area, to identify the characteristics of potential reservoirs for $CO_2$ storage, and to delineate the shaly intervals that could act as intra-formational seals. One of the well log types we used for the analysis is the spontaneous potential (SP) log. Before performing any analysis, SP logs were normalized to a common scale as SP logs are measured on a relative scale. The normalization was performed by transforming the log values into shale volume values, ranging from 0 (clean

sand) to 1 (pure shale), using the equation (Schlumberger, 1989):

$$VSH_{SP} = \frac{SP - SP_{CL}}{SP_{SH} - SP_{CL}} \quad (1)$$

where,

$VSH_{SP}$ = Shale volume from SP curve
$SP$ = Log value read from SP curve
$SP_{CL}$ = Log value in a clean sand for each well
$SP_{SH}$ = Log value in pure shale for each well

The shale volume obtained from the SP curve using the above equation was then used to determine facies for each well in the interval of interest. We assigned cut-off values to the shale volume curve to obtain a new curve with categorical values associated with different lithotypes. The cut-off values were chosen based on a multi-well histogram analysis that accounts for all of the wells in the selected area as shown below.

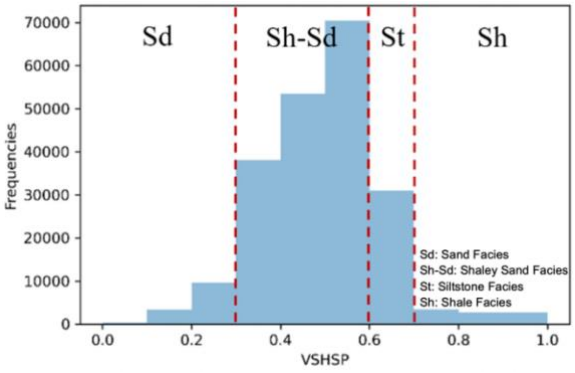


**Fig. 5.** Multiwell Histogram Analysis to determine the cutoff values for lithotypes.

**Table 1**
Lithotypes assignment

| Lithotype | Shale Volume Value Range |
|---|---|
| Sandstone | 0 – 0.3 |
| Shaly Sand | 0.3 – 0.6 |
| Siltstone | 0.6 – 0.7 |
| Shale | 0.7 - 1 |

Density porosity (DPHI) and neutron porosity (NPHI) logs were used for calculating porosity. When the bulk density log (RHOB) was the only log available, the following equation was used to transform and calculate the DPHI:

$$DPHI = \frac{\rho_B - \rho_m}{\rho_{fl} - \rho_m} \quad (2)$$

where,

$DPHI$ = Density porosity
$\rho_B$ = Bulk density measured from log
$\rho_m$ = Density of matrix (quartz = 2.65 gram/cm$^3$ [gr/cc])
$\rho_{fl}$ = Density of pore fluid (water = 1 gr/cc)

The following transformation was then used to estimate porosity from DPHI and NPHI (Alberty, 1992):

$$PHI_t = \sqrt{\frac{(NPHI^2) + (DPHI^2)}{2}} \quad (3)$$

where $PHI_t$ is the total porosity, which is a measure of the total pore space available regardless of whether it contributes to fluid flow or not. To find the fraction of the total pore volume that in fact contributes to fluid flow, which is designated as effective porosity ($PHI_e$), a transform from total porosity is applied to incorporate the shale volume obtained in the previous equations (Alberty, 1992):

$$PHI_e = PHI_t * (1 - VSH_{SP}) \quad (4)$$

After simulating the porosity values onto the geocellular grid, the porosity values in each cell of the grid can be converted into permeability values to create a new permeability model. Because we do not have any Miocene core to create a formation-specific porosity-permeability cross plot, the porosity-permeability relationship applied for this study was acquired from extrapolating a detailed study of the Frio Formation (Oligocene), Rincon Field, South Texas to the middle Miocene strata (Holtz et al., 1996; Hovorka et al., 2004). The process was carried out using the Calculator module in the DecisionSpace software and inputting the transformation equation below (Holtz, 2002):

$$k = 7 * 10^7 * \emptyset^{9.61} \quad (5)$$

where k is permeability and $\emptyset$ is the effective porosity.

### *2.3. Facies and Petrophysical Modeling*

Stratigraphic unit of MFS 6 – MFS 7 was divided into three intervals based on the normalized SP logs used for interpretation. In terms of depositional environment and sequence stratigraphy, the partition was based on the log signatures that display a couple of alternated progradational and aggradational stacking patterns. Within the interval of the area of interest, the progradational parasequence (Van

Wagoner et al., 1988) prevails near the bottom of the interval of interest. Then a set of aggradational packages follow the progradational parasequence, forming an aggradational parasequence set with a total average thickness of 400 ft. A progradational stacking pattern then starts to predominate near the top of MFS 6 eventually leading to another aggradational sequence in MFS 5 (**Fig. 6**).

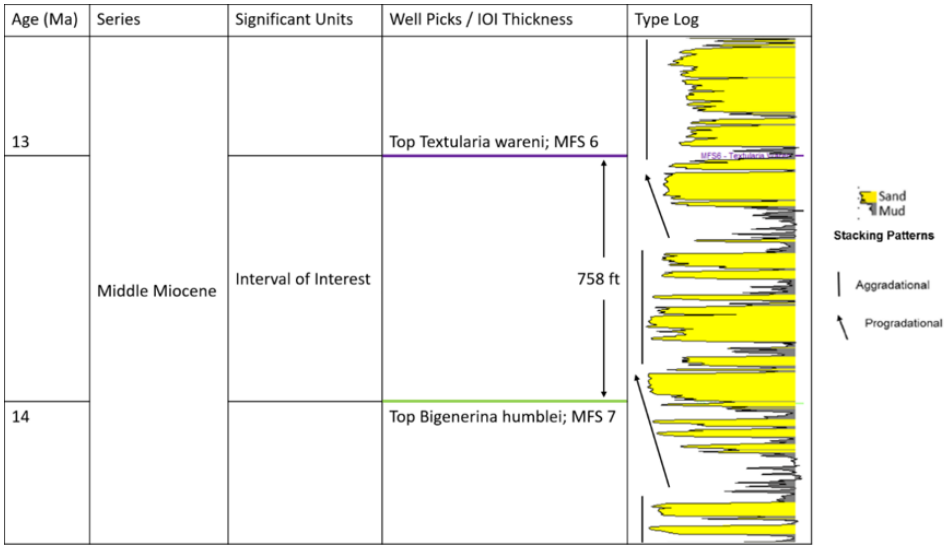


**Fig. 6.** Spontaneous potential (SP) type log showing the stacking patterns (Van Wagoner et al., 1988) of the units in the interval of interest.

We started the facies modeling process by creating a lithotype map proportion using secondary variables that define the relationship between the facies represented from the well log data. For each interval, the numbers of regions are defined based on the vertical proportion curves displayed at each well location. Once the regions are defined based on the depositional history explained at the beginning of this paper, an average proportion curve is calculated within each region.

The next step of this stage is computing variograms for each interval using previously produced proportion maps before simulating the facies onto a 3D grid using the variogram models. In this implementation, the indicator variogram is not modeled directly but instead is obtained from the facies distribution throughout the proportion maps of each interval, creating a continuous Gaussian variable (Armstrong et al., 2003). The continuous Gaussian variable is modeled and then simulated using the Turning Bands simulation algorithm and finally, the facies are obtained by applying thresholds to the Gaussian simulated values.

Lastly, we integrated the blocked point sets made from the well data that contain lithotype properties, the associated 3D stratigraphic grid, the associated proportion maps, and the facies variograms to create the facies model. This step was repeated for every interval to produce one facies model for each interval.

Additional parameters such as the depositional environment assignment for the variogram were derived from the geological history of the study area. According to Bigott (2003), Galloway (2006), and Snedden and Galloway (2019), during the middle Miocene deposode, the wave-dominated Corsair delta southwest of the study area supplies sediments into the shallow marine minibasin (also explained in Study Area and Approach section of this paper). For that reason, the wave-dominated prograding shallow marine with 45° of azimuth was chosen as the depositional environment for the lithotype rule input. The visualization of the upper part of each interval along with its lithotype percentages is shown below.

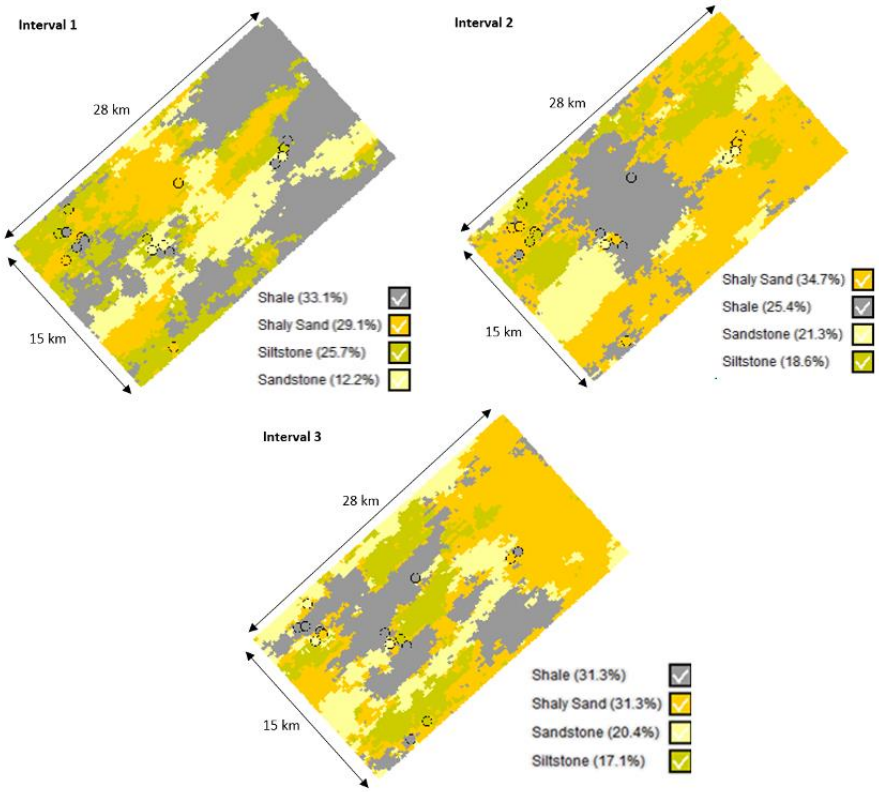


**Fig. 7.** Facies models for Interval 1 to Interval 3, showing percentages within each lithofacies.

The facies models were then populated by the Effective Porosity logs that were previously calculated using Equation (4) to produce the porosity model. Using (5), we then transformed the porosity model into a permeability model for the simulation. Table 2 shows the reservoir geometry, reservoir depth, and petrophysical properties of the model.

**Table 2**
Reservoir and fluid properties for each interval. Dipping angles were measured from base of the syncline to top of the anticline

| **Modeling Properties** | **Syncline Scenario** | **Base Scenario** |
|---|---|---|
| **Reservoir Geometry** | | |
| Average thickness (ft) | 62.65 | 50.89 |
| Surface area (km) | 28 x 15 | |
| Dipping angle (degrees) | 3° to Northeast | 5° to Northeast |
| Depth of injection point (ft) | 6,197 | 5,649 |
| **Petrophysical Properties** | | |
| Average porosity (%) | 17.85 | 17.82 |
| Porosity range (%) | 4.4 - 33.3 | 4.32 - 33.3 |
| Average permeability (mD) | 115.52 | 115.52 |
| Permeability range (mD) | 5.45 – 981 | 5.45 – 981 |

To numerically investigate how the $CO_2$ plume migrates, we ran the reservoir simulation using GEM from the Computer Modeling Group (GEM-CMG). The permeability model covered in the previous section was the input for the simulation work with a grid cell size of 750 ft in length and width and 10 ft in depth. The basic fluid properties assumed in the model are shown in Table 3, adapted from Hosseininoosheri (2019) except for the initial pressure that represents the average reservoir pressure. To model the closed boundary in the simulation model, no flow is assumed for the upper, lower, and all directions of the boundaries of the model.

**Table 3**
Fluid properties used in the simulation, modified from Hosseininoosheri (2019).

| | |
|---|---|
| **$CO_2$ Density (**lb/ft$^3$) | 37.25 |
| **Water Density (**lb/ft$^3$) | 63.16 |
| **$CO_2$ Viscosity (**cp) | 0.049 |
| **Water Viscosity (**cp) | 0.309 |
| **Initial Pressure (**psi) | 2,406 |
| **Temperature (**˚F) | 200 |

We used the Brooks and Corey (1964) water wet model for capillary pressure to model the gas and water relative permeabilities. In the following

exponential form of the Brooks and Corey model, the modified Brooks and Corey models for relative water

$$k_{rw} = k_{rw\,max}\left[\frac{S_w - S_{wc}}{1 - S_{wc} - S_{gc}}\right]^{n_w} \quad (6)$$

where,

$k_{rw}$ = Water relative permeability, value varies throughout simulation
$k_{rw\,max}$ = Maximum water relative permeability, in this case the value is 1
$S_w$ = Saturation of wetting phase, value varies throughout simulation
$S_{wc}$ = Critical saturation of water, in this case the value is 0.5
$S_{gc}$ = Critical saturation of gas, in this case the value is 0
$n_w$ = Water relative permeability exponent, in this case the value is 1.2

$$k_{rg} = k_{rg\,max}\left[\frac{S_g - S_{gc}}{1 - S_{wc} - S_{gc}}\right]^{n_g} \quad (7)$$

where,

$k_{rg}$ = Gas relative permeability, value varies throughout simulation
$k_{rg\,max}$ = Maximum gas relative permeability, in this case the value is 0.26
$S_w$ = Saturation of wetting phase, value varies throughout simulation
$S_{wc}$ = Critical saturation of water, in this case the value is 0.5
$S_{gc}$ = Critical saturation of gas, in this case the value is 0
$n_g$ = Gas relative permeability exponent, in this case the value is 6

**Fig. 8** shows the water and $CO_2$ relative permeability curve assumed for the water-wet case in this simulation.

and gas permeability are shown below:

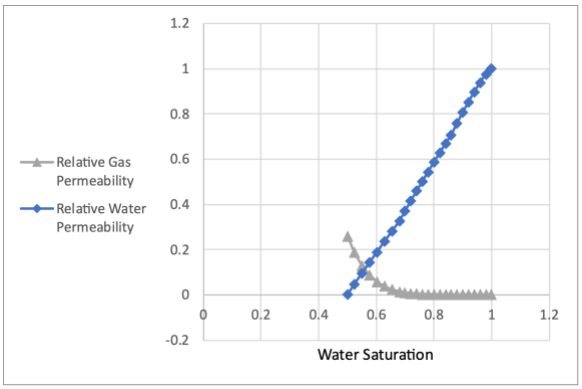


**Fig. 8.** Relative permeability curves for the simulation

We used a single capillary curve for the simulation. Changes of capillary pressure in accordance with the water saturation are shown on **Fig. 9**.

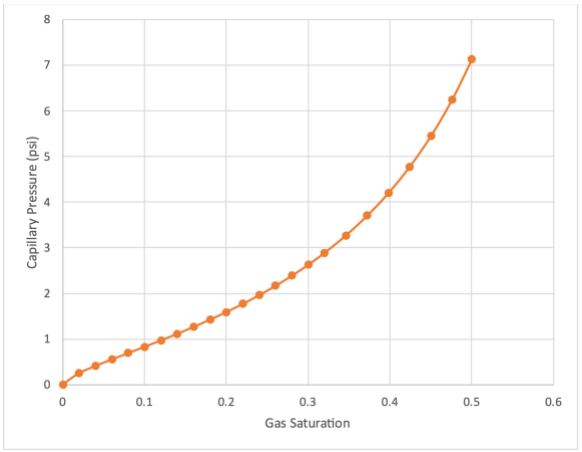


**Fig. 9.** Capillary pressure changes in accordance with water saturation

For the synclinal injection scenario, we injected the $CO_2$ at the base of the syncline as shown in the top-left image in **Fig. 10**. The high permeability strata form a migration pathway from the syncline to the anticline as seen in the top-right and bottom-left images in **Fig. 10**. As $CO_2$ is expected to migrate to the east, low permeability strata cap the storage interval as shown in the bottom-right image of **Fig. 10**.

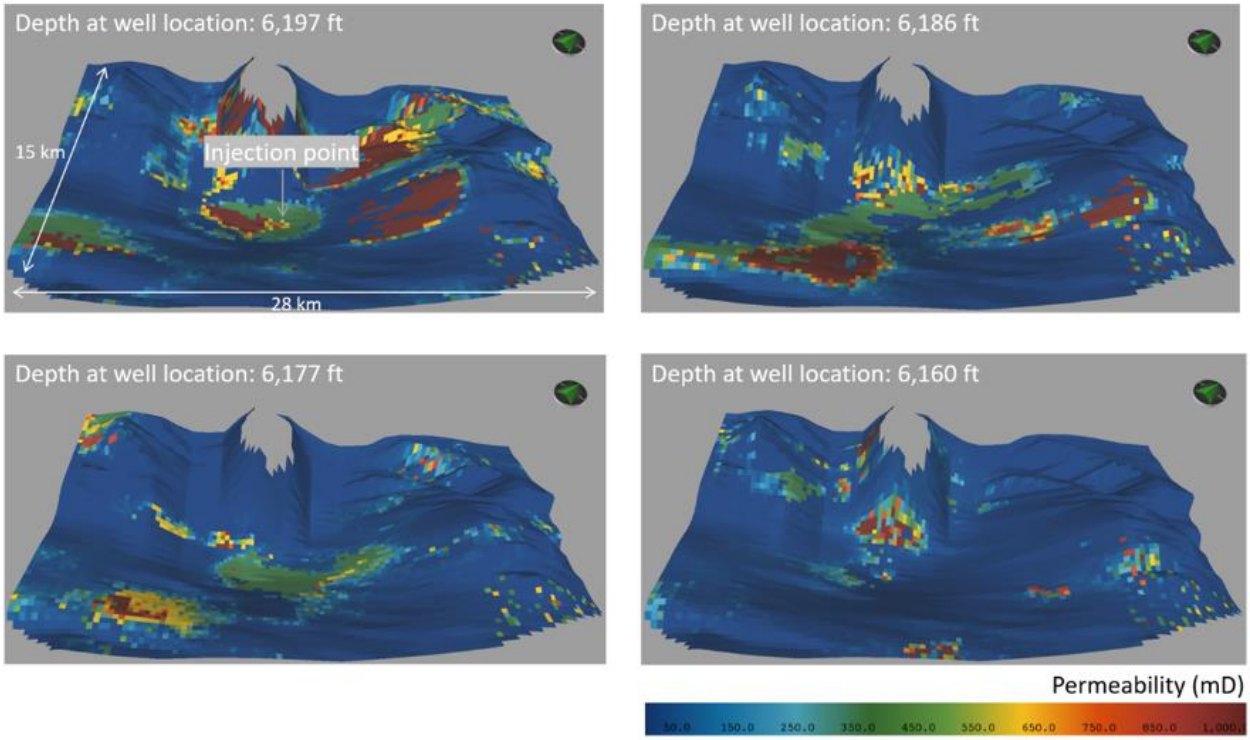


**Fig. 10.** Slices of permeability models in the synclinal injection scenario showing the variation of permeability distribution for the interval of interest (MFS 6 to 7) from the bottom of the interval of interest (upper left) to top of the interval of interest (bottom right).

For the base case scenario, we injected the $CO_2$ at the southwestern flank of the anticline as shown in the top-left image in **Fig. 11**. We expected the $CO_2$ to be distributed around the anticline area, reaching the top of it until the upward migration is limited by the low permeability strata on top of the storage interval as shown on the bottom-right image in **Fig. 11**.

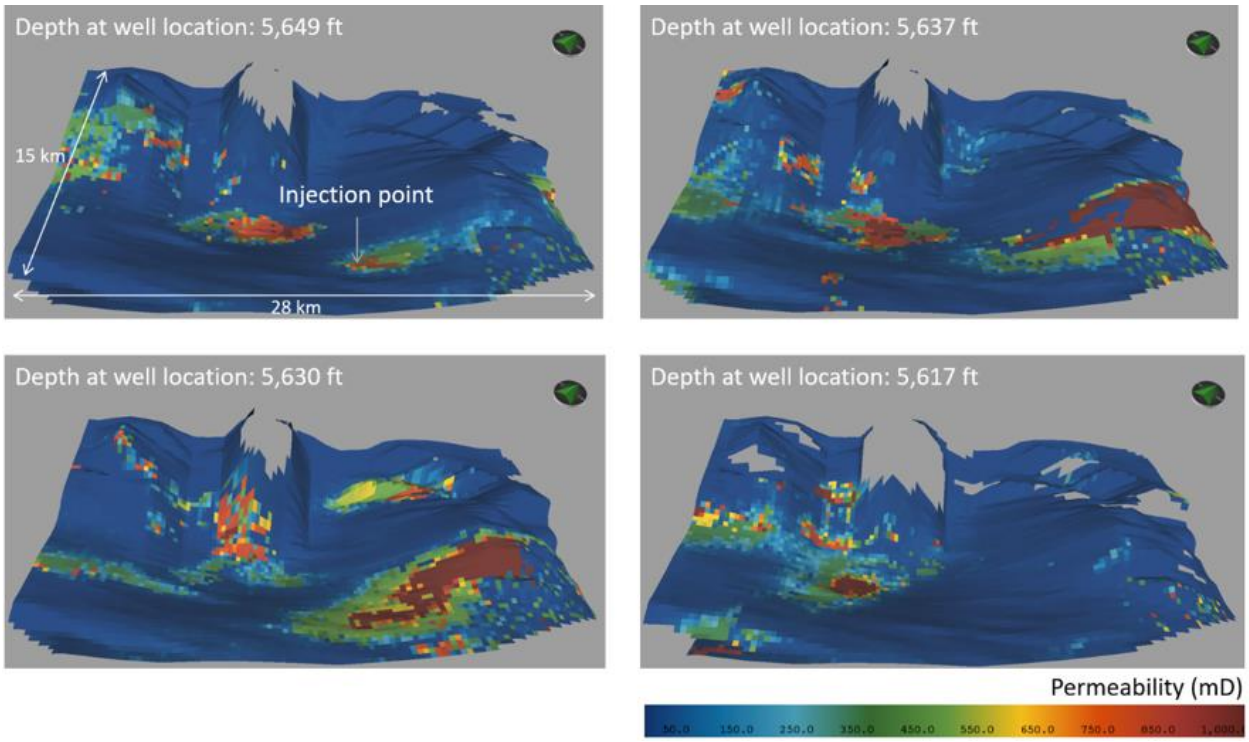


**Fig. 11.** Slices of permeability models for base case scenario showing the variation of permeability distribution for the interval of interest (MFS 6 to 7) from the bottom of the interval of interest (upper left) to the top of the interval of interest (bottom right).

In both injection scenarios, the well was designated to have a perforation of 200 ft exactly at the middle interval of the model as the average thickness of the model is 670 ft. We initially injected 1 MT of $CO_2$ per year, totaling 30 MT of $CO_2$ injected throughout the 30 years of continuous injection. However, we found from the preliminary result of the simulation that we could inject more $CO_2$ into the reservoir, therefore we created other scenarios to inject 2 MT of $CO_2$ per year, totaling 60 MT of $CO_2$ injected throughout the 30 years of continuous injection for the base scenario and the syncline scenario.

For this study, the duration of post-injection modeling was chosen as 100 years after the 30 years of continuous injection. This decision was taken based on previous research that adopted the same post-injection modeling duration (Porse, 2013; Wegner et al., 2013) and coincided with another study by Gresham et al. (2010) in the cost of leasing pore space annually examined over a 100-year time horizon.

The maximum injection pressure must be less than the fracture pressure, which is roughly 85% of the lithostatic pressure for the Gulf of Mexico (Stuart, 1960). For that reason, we adopted the value of the maximum injection pressure as 80% of the lithostatic pressure (Wallace, 2013; Garcia, 2019). For simplification, we determined the lithostatic pressure by integrating the density curve from well E located closest to the injection point of the base scenario as seen in **Fig. 11** with respect to the depth of 0 to 6,405 ft (0 to 1,952 m) using a 1-foot (0.3 meter) increment. **Figure 12** shows the best fit linear curve plotted through the data using the following equation:

$$P_{lith} = 0.94Z + 0.844 \quad (8)$$

where $P_{lith}$ is the lithostatic pressure (psi).

Maximum lithostatic pressure of 6,029 psi was obtained by using equation 8. Thus, the maximum injection pressure for the simulation is 4,823 psi (33.25 MPa).

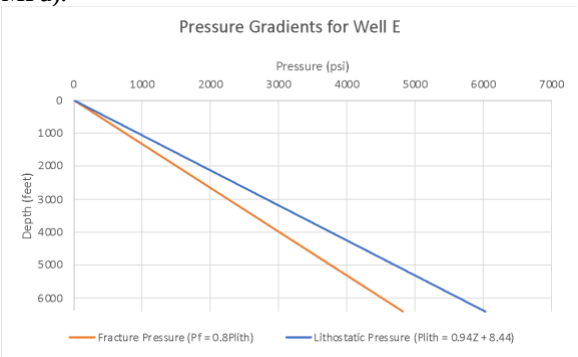


**Figure 12.** Pressure gradients used in the reservoir model

## 3. Results and Discussions

### *3.1. Plume Shape, Size, and its Evolution*

At the end of the 30 years of continuous injection of 60 MT of $CO_2$, it is observed that the plume migrates furthest, 8.46 km from the injection well in the syncline scenarios. The plume extends further as it migrates towards the anticline, reaching 10.74 km 100 years after the injection stops. Meanwhile for the same amount of $CO_2$ in the base case, in the base scenario, the plume migrates as far as 8.23 km and does not laterally migrate further after injection stops. Similar results were also observed from the 30 MT of injected $CO_2$ where the plume migrates as far as 6.40 km at the end of 30 years of continuous injection and migrates further as far as 8.69 km 100 years after the injection stops for the syncline scenario. Meanwhile, for the base scenario, the plume migrates as far as 5.94 km at the end of 30 years of continuous injection and does not laterally migrate further.

**Table 4**
Comparison study for plume migration distance in all scenarios

| Case | Plume migration distance after 30 years of continuous injection | Plume migration distance 100 years after injection stops |
|---|---|---|
| **Syncline scenario – 60 MT** | 8.46 km | 10.74 km |
| **Syncline scenario – 30 MT** | 6.40 km | 8.69 km |
| **Base scenario – 60 MT** | 8.23 km | 8.23 km |
| **Base scenario – 30 MT** | 5.94 km | 5.94 km |

Despite the greater lateral migration distance for the syncline scenario, **Fig. 13** shows that the plumes in the syncline scenario for both amounts of injected $CO_2$ do not reach the anticline at the end of 30 years of continuous injection. A very small portion of the plume from the 60 MT of injected $CO_2$ in the syncline scenario, however, reaches the anticline 100 years after the injection stops though the saturation is observed to be very low. Meanwhile, in the base scenario for both amounts of injected $CO_2$, the plumes are observed to form thick gas caps that cover the anticline completely, reaching the upper part of the anticline. It is also shown in **Fig. 14** that 100 years after injection stops, the gas saturation in the syncline scenario is observed to be approximately 0.35 and lower while the gas saturation in the base case is observed to be approximately 0.5 and mostly concentrated at the top of the anticline. The cross-sections of the base scenario also show that because plumes tend to migrate vertically rather than laterally, the parts of the storage accessed are thicker compared to the plume in the syncline scenario which tends to migrate laterally.

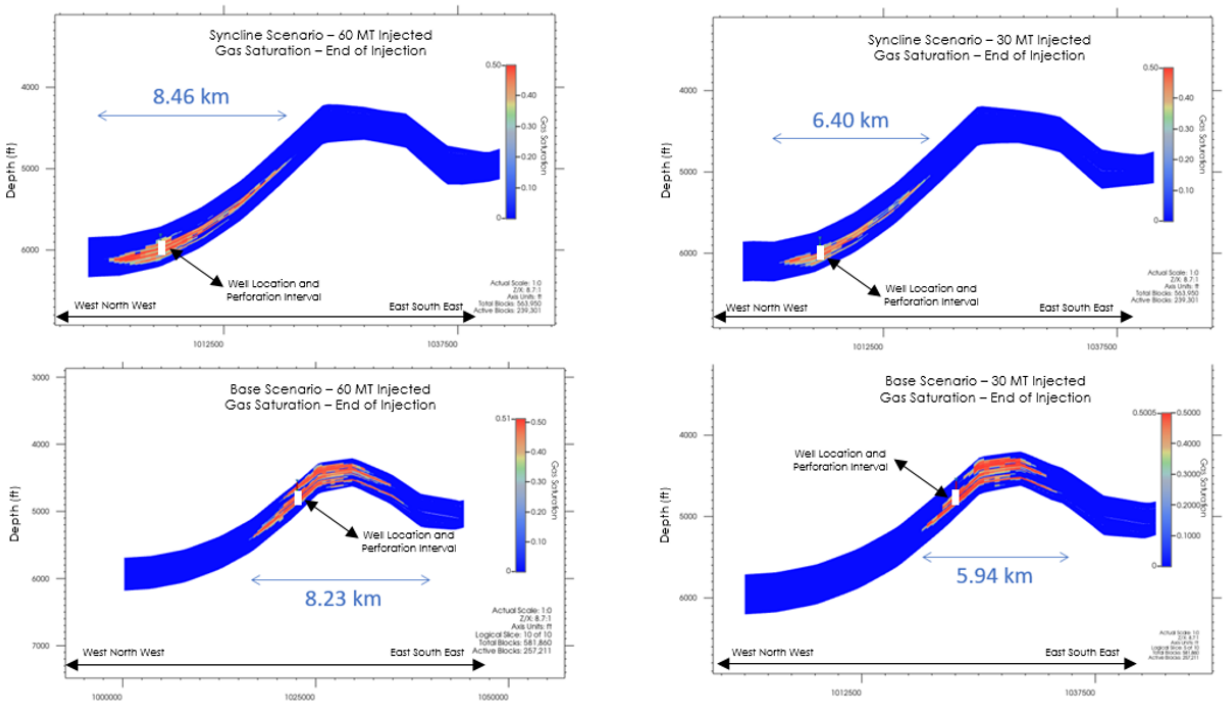


**Fig. 13.** Cross-section views of the plumes in all scenarios after 30 years of continuous injection along with each of the lateral plume migration distances.

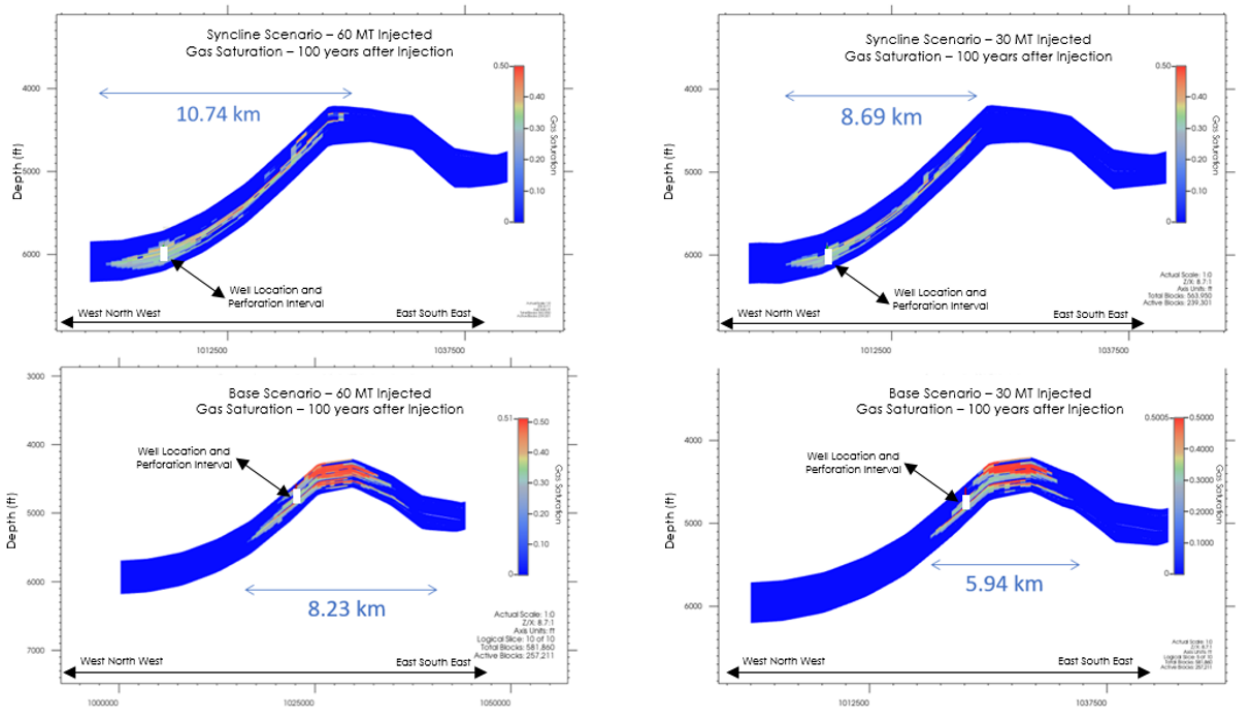


**Fig. 14.** Cross-section views of the plumes in all scenarios after 100 years after injection stops along with each of the lateral plume migration distances.

**Fig 15** shows that for the base scenario, the plume is visible at the uppermost part of the grid 30 years after continuous injection and grows even larger 100 years after injection stops. This implies that in the base case scenario, the plumes tend to migrate vertically rather than laterally and eventually reach the upper stratigraphic unit if the overlying stratigraphic layer is not impermeable enough to limit the vertical migration. Meanwhile, for the syncline scenario, no plume is visible at the uppermost part of the layer for both volumes injected at the end of 30 years of continuous injection and 100 years after the injection stops.

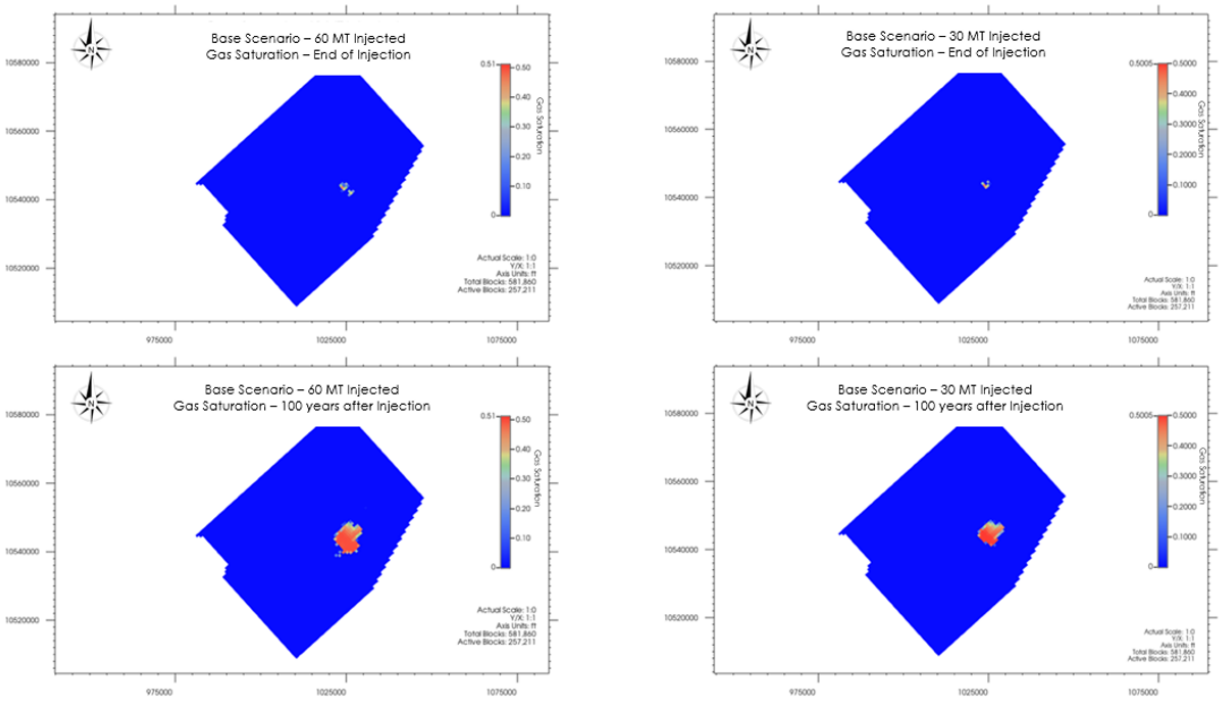


**Fig 15.** Top view of plumes in base scenario visible at the uppermost part of the grid after 30 years of continuous injection and 100 years after injection stops.

**Fig. 16** shows the top view of the plume shape for all scenarios after 30 years of continuous $CO_2$ injection. As can be seen in the figure, the differences in the plume shapes depend on the permeability distribution within the storage. The syncline scenarios show a more circular plume shape whereas the base scenarios show a more elongated plume shape.

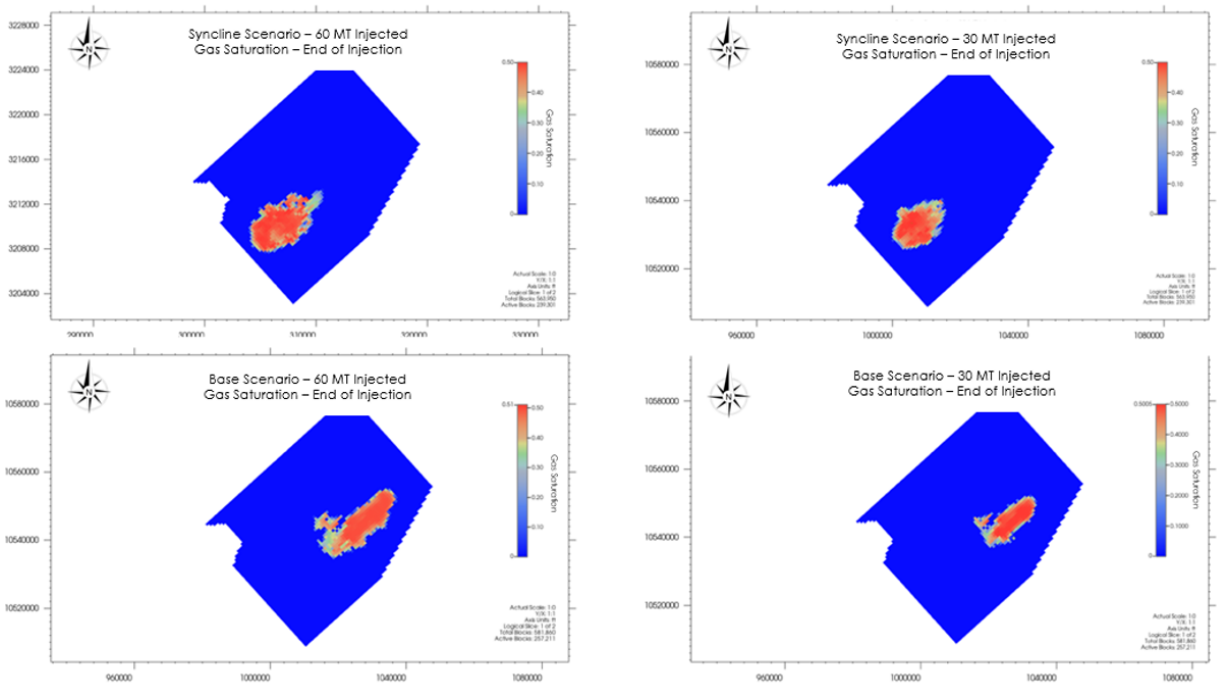


564

565 **Fig. 16.** Top view of $CO_2$ saturation after 30 years of continuous injection for all scenarios at the top of the second interval of the grid.

566 **Fig. 17** shows the top view of the plume shape for
567 all scenarios 100 years after injection stops. The upper
568 part of the figure shows the syncline scenarios. The
569 plumes appear slightly larger compared to those in the
570 previous figure, but the $CO_2$ saturations are much
571 lower. Meanwhile, for the base scenarios shown at the
572 lower part of **Fig. 17**, the plume sizes do not change but
573 relatively high values of $CO_2$ saturation still occur, and
574 they seem to be clustered around the uppermost part of
575 the anticline.

576

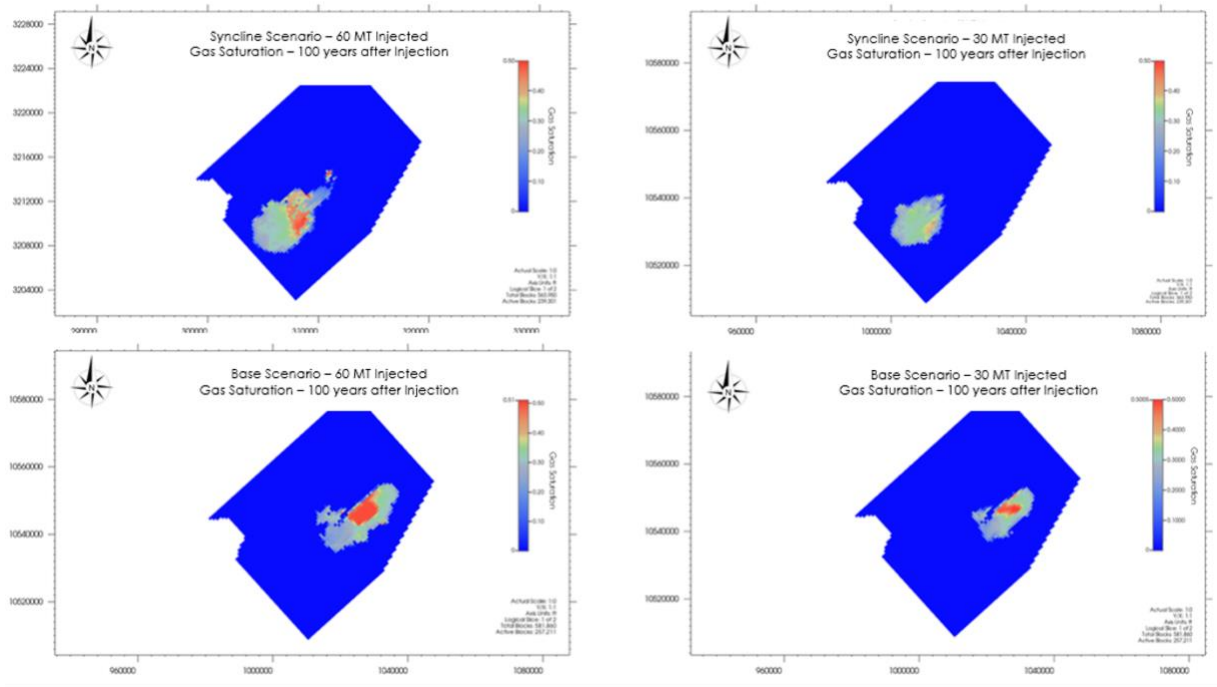


**Fig. 17.** Top view of $CO_2$ saturation 100 years after injection stops in all scenarios from the middle part of the grid.

Simulations from all scenarios show that petrophysical properties e.g. facies types, and permeability calculated from the porosity logs strongly affect the direction and extent of $CO_2$ plume movement. The similarity between the plume shape and the permeability model that is derived from colocated co-simulation between facies model and porosity logs demonstrates the importance of site characterization efforts to create a realistic geological model. The source of sediment supply during the middle Miocene deposode as discussed in Section 1 even strongly affects plume migration direction. In the anticlinal area where the storage formation is composed mostly of sand, the vertical anisotropy plays a dominant role in controlling the buoyancy flow of both light free-phase $CO_2$ and heavy dissolved-$CO_2$-laden brine. This explains why the upward plume migration tends to be more dominant in such areas. Meanwhile, in the carrier-bed-like structure, as seen in the syncline scenario where the degree of heterogeneity is higher, the sand vertical permeability is lower, and therefore there is less upward migration of $CO_2$. We conclude that the greater the degree of heterogeneity, the greater its role in diminishing the upward buoyancy flow of free-phase $CO_2$.

In the syncline scenario, the degree of heterogeneity around the injection point is higher as reflected from the distribution of lower permeability compared to the anticline area as shown in **Fig. 10**. This results in greater tortuosity of the $CO_2$ flow path, making the $CO_2$ contact more water and increasing the dissolution. This presumably is the reason why the time required for the pressure to stabilize decreases significantly as the degree of heterogeneity increases, as demonstrated in the syncline scenario. This also indicates that the lower $CO_2$ saturation resulting from greater spreading of the plume leads to more rapid residual $CO_2$ trapping. In the base scenario where the lithology around the injection point mostly consists of sandstone with a lower degree of heterogeneity, up-dip buoyancy flow is enhanced, and thus up-dip plume migration increases.

Furthermore, in the base scenario, the dominance of the sand lithotype within the storage results in a more localized flow and thus enables $CO_2$ saturation in the single plume to remain higher than in the syncline scenario. This also results in diminishing residual $CO_2$ trapping as the up-dip migration is enhanced. Dissolution trapping also decreases slightly in response to the coalescence into a single plume, as the higher $CO_2$ saturation results in a more compact plume as it approaches the cap rock on top of the anticline and thus a smaller $CO_2$ /brine contact area.

Finally, we observe the plume evolution during the injection and after the injection stops for 100 years to identify the maximum area reached by the plume. As discussed before, in the base scenario the plumes do not expand laterally after the injection stops. But in the syncline scenario, the plumes expand laterally after the injection stops as reflected from the measured

plume size and storage/acreage comparison in **Table 5**. For that reason, we calculated the storage/acreage ratios based on the plume size 100 years after the injection stops. As presented in **Table 5**, the syncline scenarios generally have a smaller storage/acreage ratio, which means that it takes larger acreage to store a certain amount of $CO_2$ with such a mechanism. On the other side, base scenarios generally have a larger storage/acreage ratio, which means that it takes smaller acreage to store a certain amount of $CO_2$ with such a mechanism.

**Table 5**
Plume size and storage/acreage ratio comparison for acreage assessment.

| Case | Total $CO_2$ injected (million tons) | Plume size after 30 years of continuous injection | Plume size 100 years after injection stops | Maximum Storage/Acreage ratio (million tons/km$^2$) |
|---|---|---|---|---|
| **Syncline scenario** | 60 | 47.66 km$^2$ | 67.73 km$^2$ | 0.88 |
| | 30 | 31.83 km$^2$ | 44.84 km$^2$ | 0.67 |
| **Base scenario** | 60 | 50.27 km$^2$ | 50.27 km$^2$ | 1.19 |
| | 30 | 26.81 km$^2$ | 26.81 km$^2$ | 1.12 |

### *3.2. Pressure Evolution*

**Fig. 18** shows the average reservoir pressure evolution from the start of injection, 30 years of continuous injection, and 100 years after injection stops for all scenarios. In all scenarios, the average reservoir pressure increases rapidly in the first 5 years of the continuous injection, and then steadily increases until it reaches its highest values at the end of the 30 years of continuous injection. The initial rapid decrease after injection end is also observed in all scenarios, followed by a very slow approach to reach the initial average reservoir pressure, which is 2406 psi, which is only nearly achieved in all scenarios 100 years after the injection stops. We adopt the stabilization definition from Doughty (2010) which directly uses $CO_2$ distributions and defines stabilization as when there is a minimum change of pressure value over time and the plume stops migrating. Simulation results show that for the base scenario, with a total of 60 million tons of $CO_2$ injected, the average reservoir pressure reaches 2,535 psi at the end of the 30-year injection period, and this value decreases rapidly and stabilizes to 2,410 psi 77 years after the injection stops. In the syncline scenario, with the same amount of injected $CO_2$, the pressure reaches 2,515 psi at the end of the 30-year injection period, and this value stabilizes to 2,410 psi 58 years after the injection stops. In both scenarios where only 30 MT of $CO_2$ is injected, it takes 20 years in the syncline scenario and 25 years in the base scenario for the average reservoir pressure to reach 2,410 psi. To summarize, the pressure decays in the syncline scenario for both amounts of $CO_2$ injected are noticeably faster than in the base scenario.

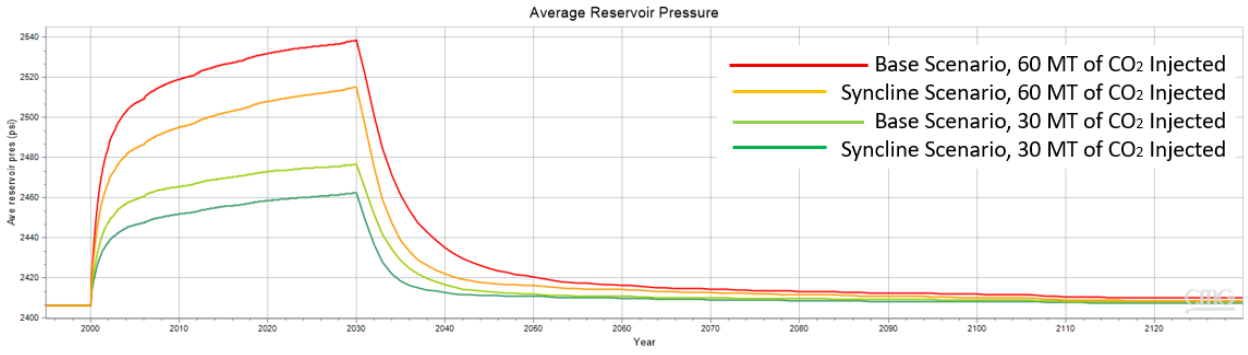


**Fig. 18.** Evolution of average reservoir pressure for all scenarios from the start of injection, 30 years of continuous injection, and 100 years after injection stops.

**Table 6**
Comparison study for stabilization time, plume migration distance, plume size, and storage/acreage ratio for each scenario

| Case | Time for the pressure to reach 2410 psi (years) | Maximum up-dip migration distance (km) | Maximum $CO_2$ plume size ($km^2$) | Storage/Acreage ratio (million tons/$km^2$) |
|---|---|---|---|---|
| **Sync-S – 60 MT** | 87 | 10.39 | 67.73 | 0.88 |
| **Sync-S – 30 MT** | 46 | 8.70 | 44.84 | 0.67 |
| **Base-S – 60 MT** | 106 | 8.41 | 50.27 | 1.19 |
| **Base-S – 30 MT** | 55 | 7.52 | 26.81 | 1.12 |

## 4. Summary, Conclusions and Recommendations

We present the results of a study integrating detailed geological characterization and reservoir simulation to measure $CO_2$ plume stabilization and the plume area referred to as the acreage needed to be leased for a $CO_2$ storage project. We investigate the behavior of $CO_2$ injected into the base of a syncline, deemed as unconventional, and at the flank of the anticline as the base case. We initially simulated the injection of 30 million tons of $CO_2$ over a 30-year period and the subsequent evolution of the $CO_2$ plume for 30 years in the two scenarios. Reservoir simulation results indicate that the injected $CO_2$ plume is effectively immobilized at 20 years with the syncline scenario. The plume footprints from both scenarios resemble the permeability model and extend much farther up-dip of the injection well than down-dip. Furthermore, we doubled the amount of $CO_2$ injected, and it increases the plume sizes for both scenarios. For comparison, the ratio of the injected amount of $CO_2$ and maximum plume size is 1.19 MT/$km^2$ for the base case and 0.88 MT/$km^2$ for the syncline case with the 60 MT of $CO_2$ injected.

The pressure responses decrease rapidly with distance from the injection well and decay rapidly in time once injection ceases. Moreover, the post-injection pressure decreases in the syncline scenario are noticeably faster than those in the base scenario. We conclude that, provided we have a geologic area similar to the syncline scenario, by utilizing the syncline scenario, we need a slightly larger area to store $CO_2$ compared to the base scenario, but a significantly faster plume stabilization time will result.

Our comparison study between the two injection scenarios demonstrates that geological properties have a large impact on plume evolution, causing significant trade-offs between different injection mechanisms. The minibasin that is connected to the anticline in the offshore Galveston, Gulf of Mexico area, as visualized in the syncline scenario of this study resembles the migration pathway in the petroleum system. The simulation shows the ratio between the amount of $CO_2$ injected and the plume size for the syncline scenario is generally smaller than the base case. This means that by injecting the $CO_2$ into a syncline, we need more acreage to be leased rather than injecting $CO_2$ at the flank of the anticline for the same amount of $CO_2$. The reason why the syncline mechanism takes more acreage is that the geological layer around the injection point is more heterogeneous than the base scenario, thus making the $CO_2$ tend to migrate laterally. On the positive side, the study also shows that interleaved sands and shale lithology along the migration pathway are likely to increase the retention of $CO_2$ in the subsurface. Such a mechanism also limits the vertical migration of $CO_2$, thus making the syncline mechanism bear a lower risk for the $CO_2$ to escape to the upper geological layers. Furthermore, the average reservoir pressure tends to dissipate and decay faster in the syncline scenario, which could result in a decrease in monitoring frequency as the project runs. To summarize, conclusions about the plume migration and trapping mechanisms drawn from this study by comparing all of the scenarios presented may be widely useful as one of the geologic parameters to screen for favorable storage locations.

## Acknowledgement

The authors are grateful to anonymous reviewers and BEG internal reviewers. We gratefully acknowledge Halliburton for the use of the Landmark Graphics interpretation software provided under the Landmark University Grant Program to The University of Texas at Austin. Our gratitude is extended to the Computer Modeling Group, Calgary, Canada (CMG) for providing CMG-GEM and associated software. We are also grateful to Seismic Exchange Inc. for providing the OBS seismic dataset for this work. This work was supported by the GoMCarb project, funded by the U.S. Department of

Energy, NETL, under award number DE-FE0031558. Publication authorized by the Director, Bureau of Economic Geology, Jackson School of Geosciences, The University of Texas at Austin.

## Disclaimer

This report was prepared as an account of work sponsored by an agency of the United States Government. Neither the United States Government nor any agency thereof, nor any of their employees, makes any warranty, express or implied, or assumes any legal liability or responsibility for the accuracy, completeness, or usefulness of any information, apparatus, product, or process disclosed, or represents that its use would not infringe privately owned rights. Reference herein to any specific commercial product, process, or service by trade name, trademark, manufacturer, or otherwise does not necessarily constitute or imply its endorsement, recommendation, or favoring by the United States Government or any agency thereof. The views and opinions of authors expressed herein do not necessarily state or reflect those of the United States Government or any agency thereof.

## References

Alberty, M. 1992. Standard Interpretation: Part 4. Wireline Methods.

Beckham, E. C. 2018. $CO_2$ storage in deltaic environments of deposition: integration of 3-dimensional modeling, outcrop analysis, and subsurface application (Master's Thesis). The University of Texas at Austin. Austin, Texas.

Bradshaw, B. E., and Watkins, J. S.. 1994. Growth-fault evolution in offshore Texas. In: Gulf Coast Association of Geological Societies Transactions, v. 44, p. 103-110.

Cavanagh, A. J., Haszeldine, R. S, 2014. The Sleipner storage site: Capillary flow modeling of a layered CO2 plume requires fractured shale barriers within the Utsira Formation. In: International Journal of Greenhouse Gas Control, v. 21, p. 101-112. https://doi.org/10.1016/j.ijggc.2013.11.017.

Combellas-Bigott RI, Galloway WE. 2006. Depositional and structural evolution of the middle Miocene depositional episode, east-central Gulf of Mexico. AAPG Bulletin, v. 90, no. 3, 335–362. https://doi.org/10.1306/10040504132

Diegel, F. A., Karlo, J. F., Schuster, D. C., Shoup, R.C., and Tauvers, P. R. 1995. Cenozoic structural evolution and tectonostratigraphic framework of the north-ern Gulf Coast continental margin. In: Salt Tectonics: A Global Perspective. American Association of Petroleum Geologists, Tulsa, Memoir, 65, 109–151. https://doi.org/10.1306/M65604C6

Doughty, C. 2010. Investigation of $CO_2$ plume behavior for a large-scale pilot test of geologic carbon storage in a saline formation. Transport in Porous Media 82, 49–76. https://doi.org/10.1007/s11242-009-9396

Holtz M, H. 2002. Residual gas saturation to aquifer influx: a calculation method for 3-D computer reservoir model construction. In: The SPE Gas Technology Symposium, Calgary. doi:10.2118/75502-MS

Hosseininoosheri P. 2019. $CO_2$ trapping mechanisms assessment using numerical and analytical methods (Dissertation). The University of Texas at Austin. Austin, Texas.

Hovorka, S., Doughty, C., Benson, S., Pruess, K., and Knox, P.. 2004. The impact of geological heterogeneity on $CO_2$ storage in brine formations: a case study from the Texas Gulf Coast. In Geological Storage of Carbon Dioxide, 147-163. The Geological Society of London. https://doi.org/10.1144/GSL.SP.2004.233.01.10

Hudec, M.R., Jackson, M.P.A., Schultz-Ela, D.D. 2009. The paradox of minibasin subsidence into salt: clues to the evolution of crustal basins. In Geological Society of America Bulletin, vol. 121, 201-221. https://doi.org/10.1130/B26275.1

Jackson, M., & Hudec, M. 2017. Salt Tectonics: Principles and Practice. Cambridge: Cambridge University Press.

Ni, P., Boon, M., Garing, C., and Benson, S. 2019. Predicting $CO_2$ residual trapping ability based on experimental petrophysical properties for different sandstone types. In International Journal of Greenhouse Gas Control, vol. 86, 158-176. https://doi.org/10.1016/j.ijggc.2019.04.024

Peel F. J. 2014. How do salt withdrawal minibasins form? Insights from forward modelling, and implications for hydrocarbon migration. Tectonophysics 630, 222–235. https://doi.org/10.1016/j.tecto.2014.05.027

Ramberg, H. 1981. The role of gravity in orogenic belts. In Special Publications of the Geological Society of London, vol. 9, 125-140. https://doi.org/10.1144/GSL.SP.1981.009.01.11

Schlumberger. 1989. Log Interpretation Principles/Applications.

Snedden, J., & Galloway, W. 2019. Cenozoic depositional history 2: Middle Cenozoic geothermal phase. In the Gulf of Mexico Sedimentary Basin: Depositional Evolution and Petroleum Applications (pp. 191-210). Cambridge: Cambridge University Press. doi:10.1017/9781108292795.010

Trevisan, L., R. Pini, A. Cihan, J. T. Birkholzer, Q. Zhou, A. Gonzalez-Nicolas, and T. H. Illangasekare 2016. Imaging and quantification of spreading and trapping of carbon dioxide in saline aquifers using meter-scale laboratory experiments. In: Water Resources Research, 53, 485–502. https://doi.org/10.1002/2016WR019749

Van Wagoner, J. C., Posamentier, H. W., Mitchum, R. M. J., Vail, P. R., Sarg, J. F., Loutit, T. S., & Hardenbol, J. (1988). An overview of the fundamentals of sequence stratigraphy and key definitions. In Sea-Level Changes: An Integrated Approach. SEPM Special Publication 42, Darlington, 39-45. https://doi.org/10.2110/pec.88.01

Zhang F, Miao S, Wang, W, Huang Y, Zhou B, Loggia D, Vasseur G. (2006). Experimental verification of oil saturation and loss during secondary migration. Journal of Petroleum Geology. 27. 241 - 251. 10.1111/j.1747-5457.2004.tb00057